Redox Biology 61 (2023) 102627

Contents lists available at ScienceDirect

Redox Biology

journal homepage: www.elsevier.com/locate/redox

NADK-mediated *de novo* NADP(H) synthesis is a metabolic adaptation essential for breast cancer metastasis

Didem Ilter [a,1], Stanislav Drapela [a,1], Tanya Schild [b,1], Nathan P. Ward [c], Emma Adhikari [d], Vivien Low [e,f], John Asara [g], Thordur Oskarsson [a], Eric K. Lau [d], Gina M. DeNicola [c], Melanie R. McReynolds [h,i], Ana P. Gomes [a,*]

[a] Department of Molecular Oncology, H. Lee Moffit Cancer Center & Research Institute, Tampa, FL, USA
[b] Department of Radiology, Memorial Sloan Kettering Cancer Center, New York, NY, USA
[c] Department of Cancer Physiology, H. Lee Moffit Cancer Center & Research Institute, Tampa, FL, USA
[d] Department of Tumor Biology, H. Lee Moffit Cancer Center & Research Institute, Tampa, FL, USA
[e] Department of Pharmacology, Weill Cornell Medicine, New York, NY, USA
[f] Meyer Cancer Center, Weill Cornell Medicine, New York, NY, USA
[g] Mass Spectrometry Core, Beth Israel Deaconess Medical Center, Boston, MA, USA
[h] Department of Biochemistry and Molecular Biology, Penn State University, University Park, PA, USA
[i] Huck Institutes of the Life Sciences, Penn State University, University Park, PA, USA

ARTICLE INFO

Keywords:
Metastasis
Breast cancer
Redox
NADPH
NADK

ABSTRACT

Metabolic reprogramming and metabolic plasticity allow cancer cells to fine-tune their metabolism and adapt to the ever-changing environments of the metastatic cascade, for which lipid metabolism and oxidative stress are of particular importance. NADPH is a central co-factor for both lipid and redox homeostasis, suggesting that cancer cells may require larger pools of NADPH to efficiently metastasize. NADPH is recycled through reduction of $NADP^+$ by several enzymatic systems in cells; however, *de novo* $NADP^+$ is synthesized only through one known enzymatic reaction, catalyzed by NAD^+ kinase (NADK). Here, we show that NADK is upregulated in metastatic breast cancer cells enabling *de novo* production of NADP(H) and the expansion of the NADP(H) pools thereby increasing the ability of these cells to adapt to the challenges of the metastatic cascade and efficiently metastasize. Mechanistically, we found that metastatic signals lead to a histone H3.3 variant-mediated epigenetic regulation of the NADK promoter, resulting in increased NADK levels in cells with metastatic ability. Together, our work presents a previously uncharacterized role for NADK and *de novo* NADP(H) production as a contributor to breast cancer progression and suggests that NADK constitutes an important and much needed therapeutic target for metastatic breast cancers.

1. Introduction

Breast cancer is the most common malignancy that affects Western women. While the primary tumour can be treated by surgery and adjuvant therapy, metastases are a major cause of mortality [1–3]. Thus, the ability to effectively treat solid tumors is largely dependent on the capacity to prevent and/or treat metastatic disease. Metastasis is a complex process in which cancer cells escape the primary tumour, invade the adjacent tissue, enter, and survive in circulation and eventually colonize distant sites [1–3]. As such, cancer cells that go through the metastatic cascade need to overcome many obstacles and adapt to many different environments to retain vitality and eventually thrive as metastatic lesions.

One of the most striking distinctions between tumors and non-transformed tissues are the differences in their metabolism [4,5]. These differences have been used to diagnose tumors, such as the use of ^{18}F-fluorodeoxyglucose PET imaging [6], and have been considered a hallmark of cancer [7]. Recent reports made it clear that metabolic alterations are not just a pivotal player in primary tumors but are also required for metastases. Indeed, alterations in glucose metabolism were shown to provide a metabolic advantage in basal-like breast cancer [8]. Moreover, the ability of certain tumors to metastasize was shown to be highly dependent on metabolic pathways such as the folate cycle [9] and

* Corresponding author.
E-mail address: ana.gomes@moffitt.org (A.P. Gomes).
[1] Equal Contribution.

https://doi.org/10.1016/j.redox.2023.102627
Received 8 January 2023; Received in revised form 30 January 2023; Accepted 2 February 2023
Available online 9 February 2023

Abbreviations

BME	basal-membrane extract
ChIP-seq	chromatin immunoprecipitation sequencing
EMT	epithelial-to-mesenchymal transition
G6PD	glucose-6-phosphate dehydrogenase
IDH	isocitrate dehydrogenase
ME	malic enzyme
NAC	N-acetylcysteine
NAD^+	nicotinamide adenine dinucleotide
NADK	NAD^+ kinase
$NADP^+$	nicotinamide adenine dinucleotide phosphate
NADPH	reduced NADP
NAM	nicotinamide
redox	reduction-oxidation
ROS	reactive oxygen species
TNBC	triple negative breast cancer
TPNOX	triphosphopyridine nucleotide oxidase

the pyrimidine metabolism [10]. Much of the metabolism in cancer cells serves to support anabolic and reduction-oxidation (redox) reactions that generate building blocks needed to maintain high rates of proliferation without inducing cell death due to accumulation of reactive oxygen species (ROS). Metabolic reprogramming and metabolic plasticity provide cancer cells with the flexibility necessary to withstand the challenges provided by the ever-changing environments of the metastatic cascade and power the development of metastatic disease [11,12]. Lipid metabolism and oxidative stress are of particular importance in the metastatic cascade [11,13–16]. In fact, disruption of either lipid or redox homeostasis has profound effects in the ability of cancer cells to thrive as metastases [9,17–20].

A cornerstone of both lipid and redox homeostasis is nicotinamide adenine dinucleotide phosphate ($NADP^+$) and reduced NADP (NADPH) metabolism. NADP(H) is an essential cofactor used for transferring and reserving reduction potential, which is used to power biosynthetic pathways (including lipid synthesis) as well as redox homeostasis [21]. Since NADPH is a central electron donor to anabolic reactions and antioxidant systems, its generation is vital for the ability of cells to grow, proliferate and survive. Similarly to glutathione, it cycles between reduced (NADPH) and oxidized states ($NADP^+$), with several enzymes having a key role in its regeneration. NADPH can be recovered by several metabolic enzymes in the cell, including glucose-6-phosphate dehydrogenase (G6PD), isocitrate dehydrogenase (IDH), malic enzyme (ME) and folate cycle-related enzymes [21]. Importantly, while reactions that catalyze the recycling of NADPH and $NADP^+$ are well characterized in mammalian systems, reactions mediating the *de novo* synthesis of these reducing equivalents are not. NADPH is not known to be *de novo* produced in humans. However, $NADP^+$ can be *de novo* synthesized in cells through a single enzymatic reaction that adds a phosphate moiety from a nucleotide donor, typically ATP, onto the 2' position of NAD^+ [21]. Interestingly, it has been previously shown that circulating tumor cells that successfully formed metastatic nodules had elevated levels of NADPH [9], suggesting that increased NADPH is needed to fuel the metabolic and redox demands of the metastatic cascade and enable successful colonization of distal organs. Yet, very little is known about how NADP(H) homeostasis and the heightened need for NADP(H) are maintained through the breast tumorigenic process, particularly as they progress into metastatic disease.

2. Results and discussion

2.1. De novo NADP(H) generation is upregulated in breast cancer metastasis

Considering the importance of redox balance for metastasis [9] and the central role of NADPH in enabling redox homeostasis we questioned if maintaining NADPH levels is important for breast cancer metastasis. To test this, we expressed triphosphopyridine nucleotide oxidase (TPNOX) in the highly metastatic 4T1 triple negative breast cancer (TNBC) model. TPNOX is an engineered mutant of the naturally occurring *Lactobacillus brevis* NADH oxidase that is strictly specific towards NADPH and whose expression leads to NADPH oxidation into $NADP^+$ thereby decreasing NADPH availability [22]. To evaluate the effects of TPNOX expression on the metastatic ability of 4T1 cells, we grew these cells in 3D conditions, which have been shown to be a better environment than 2D growth to promote the metabolic alterations that occur in metastasis [23]. TPNOX expression severely blunted the ability of these cells to grow in soft agar (Fig. 1a), demonstrating the importance of NADPH for the 3D growth and metastatic potential of these cells. Based on these results, we hypothesized that breast cancer cells may hijack pathways that reduce $NADP^+$ into NADPH to maintain the NADPH levels necessary for 3D growth and efficient metastasis. To test this we first took advantage of clonal subpopulations, which were isolated from a 4T1 mammary tumor and display different metastatic abilities [24], to measure $NADP^+$ and NADPH levels. NADPH levels were significantly higher in the broadly metastatic 4T1 clone, which can form metastases, compared to a locally invasive 4T07 clone, which can invade out of the primary tumor but fails to form metastases (Fig. 1b). Unexpectedly, we observed no change in $NADP^+$ levels (Fig. 1c) putting forward the idea that metastasis formation might be dependent on the ability of breast cancer cells to increase their total NADP(H) pools. In support of this idea, we observed that both $NADP^+$ and NADPH levels are upregulated in metastases arising from orthotopic implantation of 4T1 cells into the mammary fat pad when compared to their levels in the primary tumors (Fig. 1d and e). Changes in the total NADP(H) pools are regulated by *de novo* NADP(H) synthesis, via phosphorylation of nicotinamide adenine dinucleotide (NAD^+) to form $NADP^+$, which is catalyzed by NAD kinases (NADKs) [21]. To evaluate if indeed metastatic proficient cells have higher rates of *de novo* NADP(H) synthesis we traced the incorporation of isotopic label from deuterated nicotinamide, [2,4,5,6-^{2}H]NAM, into the NADP(H) pools using a previously developed method [25] optimized for this specific context (Fig. S1a). We observed increased label incorporation into the $NADP^+$ and NADPH pools of the 4T1 clone when compared to the 4T07 clone (Fig. 1f and g), demonstrating that *de novo* NADP(H) synthesis is increased in breast cancer cells with the ability to effectively metastasize and suggesting that NADKs might be an important point of regulation to enable tumor progression.

2.2. NADK is upregulated in breast cancer metastasis

Mammalian *de novo* NADP(H) synthesis can be catalyzed by two NADK isoforms, a cytosolic (NADK) and a mitochondrial one (NADK2) [21] (Fig. 1h). Considering that the increase in ROS in disseminated cancer cells was previously shown to occur in the cytosol before it propagates to both cytosol and mitochondria in metastatic lesions [9] as well as the fact that fatty acid synthesis occurs in the cytosol, we reasoned that the cytosolic NADK might be responsible for the increase in *de novo* NADP(H) synthesis observed in our experiments. In support of this idea, we observed that NADK levels are increased in the metastatic proficient 4T1 clone compared to the 4T07 clone that cannot effectively metastasize (Fig. 1i). Moreover, we observed the same trend in NADK levels when comparing human breast cancer cell lines derived from metastatic and non-metastatic sites (Fig. 1j). Evaluation of human breast cancer samples showed an increase in NADK levels in metastases versus their matched primary tumors (Fig. 1k) demonstrating that NADK

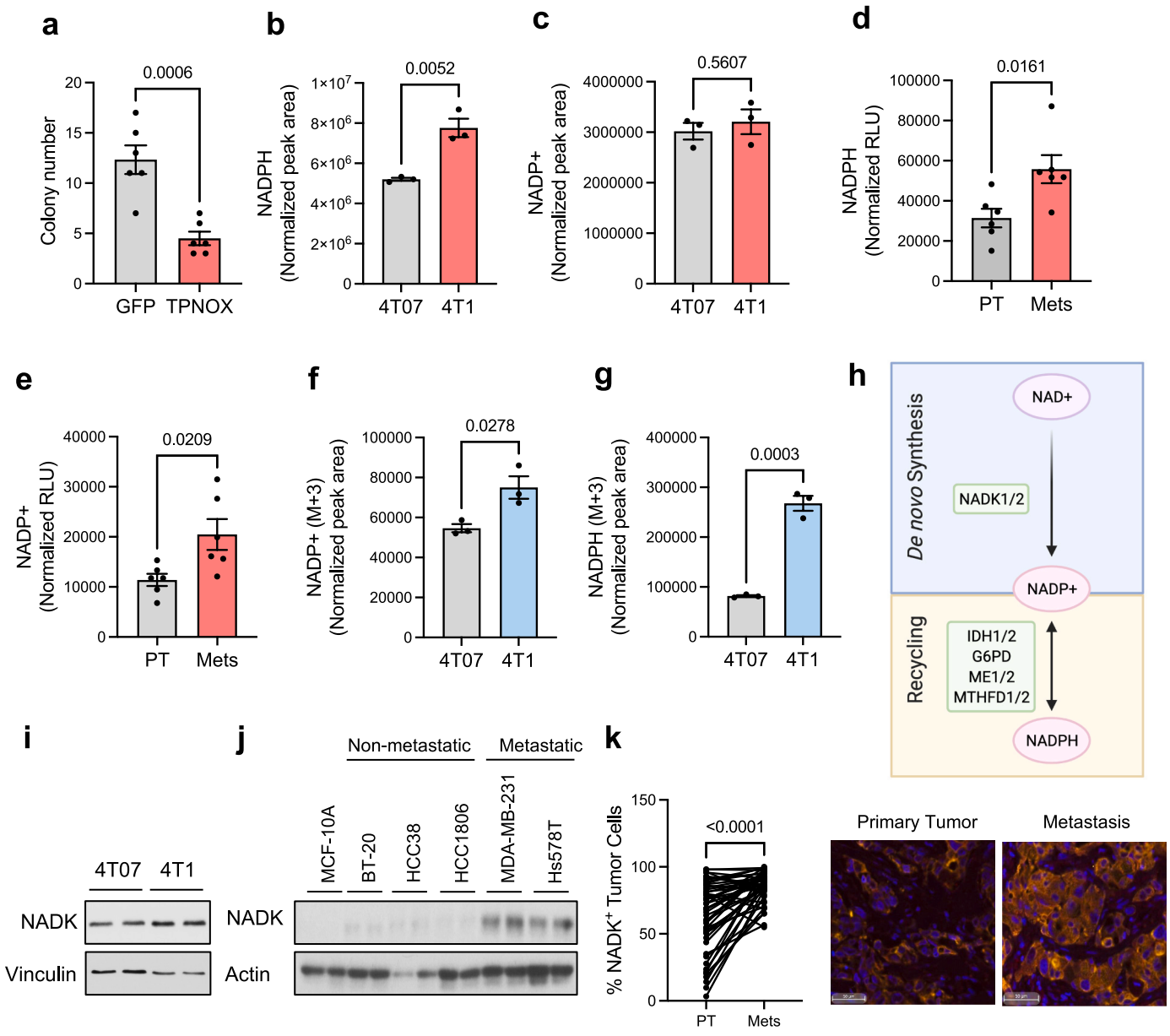

Fig. 1. *De novo* $NADP^+$ synthesis is upregulated in metastatic breast cancer cells. a, Soft agar colony formation assay in 4T1 cells expressing TPNOX or GFP (n = 6). **b, c,** NADPH **(b)** and $NADP^+$ **(c)** levels in 4T1 (broadly metastatic) and 4T07 (locally invasive) clones (n = 3). **d, e,** NADPH **(d)** and $NADP^+$ **(e)** levels in 4T1-derived primary tumors (PT) or lung metastases (Mets; n = 6). **f, g,** *De novo* $NADP^+$ **(f)** and NADPH **(g)** production from labelled NAM in 4T1 and 4T07 clones (n = 3). **h,** Schematic representation of NADP(H) synthesis and recycling. **i, j,** NADK immunoblot in 4T1 and 4T07 **(i)**, and in breast epithelial cells, non-metastatic breast cancer cells and metastatic breast cancer cells **(j)**; representative image (n = 4). **k,** Percentage of cells positive for NADK in human breast cancer primary tumor samples and matched metastases (n = 50) and representative images. All values are expressed as mean ± SEM.

upregulation is a feature of human breast cancer metastasis. Although we cannot exclude a role of NADK2, our data point for the direct relevance of *de novo* NADP(H) synthesis catalyzed by NADK in the cytosol to the progression of breast cancers into a metastatic state.

2.3. *NADK is essential for breast cancer metastatic cells to maintain their NADP(H) pools and their metastatic capacity*

Having shown that total NADP(H) pools and NADK levels are elevated in breast cancer metastases, we next probed its functional consequences. To test this, we silenced NADK in 4T1 cells as well as in a human cell line with high metastatic ability (MDA-MB-231 LM2 [26], referred to as LM2 hereafter). NADK silencing in both 4T1 and LM2 cells resulted in decreased total NADP(H) levels while having no consistent effects on NAD^+ levels (Figs. S1b–f, Fig. 2a and b), Similarly, while no change in the production of NAD^+ from [2,3,5,6-^{2}H]NAM is consistently observed (Figs. S1g and h), *de novo* synthesis of $NADP^+$ is significantly hampered in both 4T1 and LM2 cells (Fig. 2c and d). Supporting the importance of *de novo* $NADP^+$ synthesis for metastatic-like growth, we observed that NADK suppression in 4T1 or LM2 cells resulted in a pronounced decrease in their ability to grow in 3D, both in soft agar (Fig. 2e and f) and in the presence of an extracellular matrix hydrogel, basal-membrane extract (BME) (Figs. S2a and b). Conversely, overexpression of NADK in a non-metastatic breast cancer cell line increased $NADP^+$ levels and promoted their ability to grow in 3D (Figs. S2c–e), suggesting that NADK is an important regulator of metastatic outgrowth. To evaluate how NADK might impact metastasis formation we performed lung colonization assays; NADK suppression drastically reduced

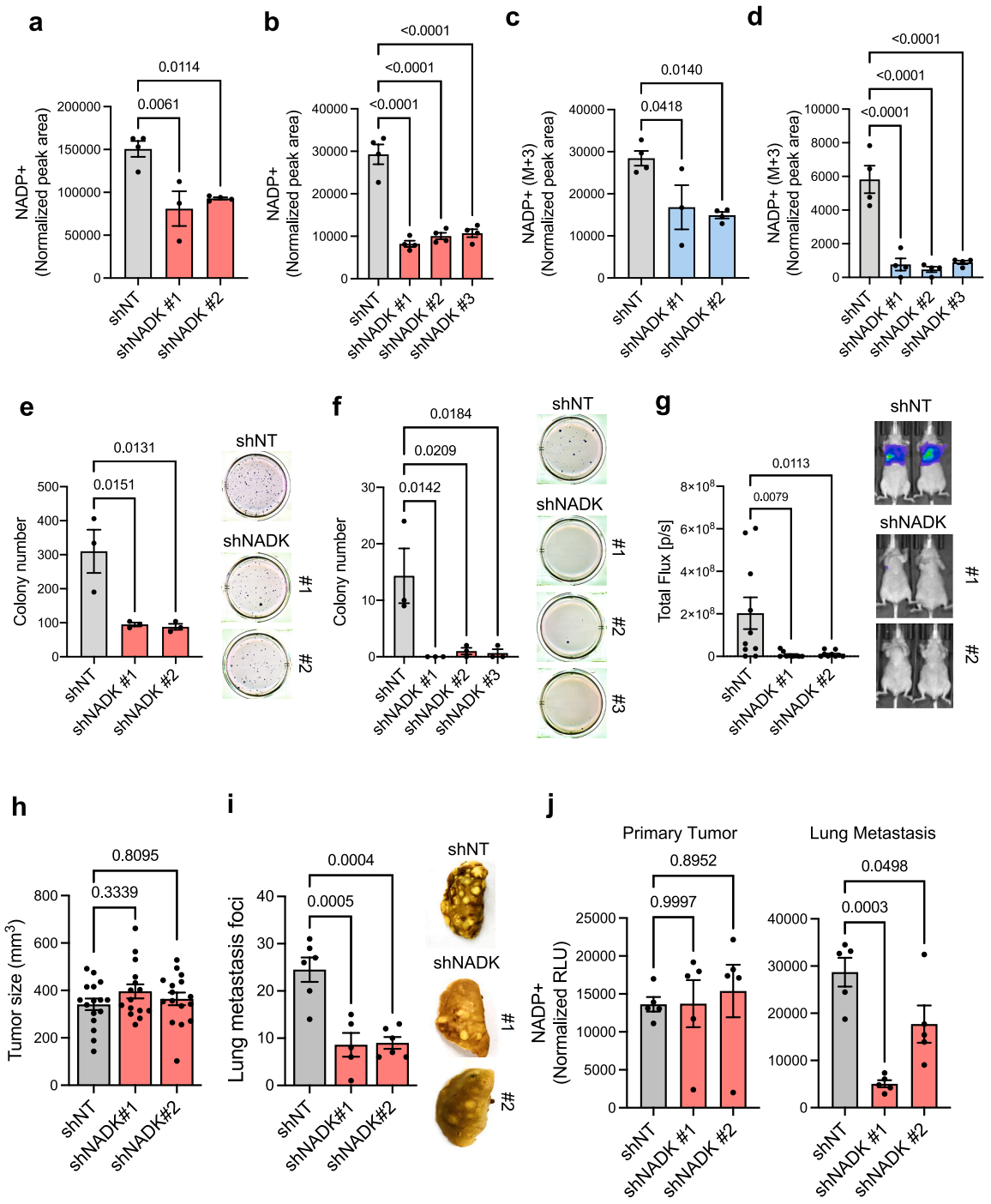

Fig. 2. NADK mediates *de novo* $NADP^+$ synthesis and enables breast cancer lung metastasis. a, b, $NADP^+$ levels in 4T1 cells **(a)** and LM2 cells **(b)** with NADK knockdown for 3 days (n = 3). **c, d,** *De novo* $NADP^+$ production from labelled NAM in 4T1 cells **(c)** and LM2 cells **(d)** with NADK knockdown for 3 days (n = 4). **e, f,** Quantification, and representative images, of soft agar colony formation assay in 4T1 **(e)** and LM2 cells **(f)** with NADK knockdown (n = 3). **g,** Lung colonization assay of LM2 cells with knockdown of NADK (n = 10). **h-j,** Primary tumor size (n = 16) **(h),** number of lung metastasis foci (n = 6) **(i)** and $NADP^+$ levels **(j)** in the primary tumor and metastatic lesions of 4T1 syngeneic model with knockdown of NADK. All values are expressed as mean ± SEM.

the ability of LM2 cells to effectively colonize the lung following a tail-vein injection (Fig. 2g). Moreover, orthotopic implantation of 4T1 cells with NADK suppressed in an immune competent mouse revealed that the effect of NADK is restricted to metastasis as knockdown of NADK has no effect in primary tumor growth while reducing lung metastatic burden (Fig. 2h and i). Evaluation of NADP(H) levels showed that NADK suppression has no effect on $NADP^+$ or NADPH levels in the primary tumor but significantly reduces NADP(H) levels in lung metastasis (Fig. 2j, Fig. S2f). This observation suggests that a dichotomy exists in the regulation of NADP(H) pools between the primary tumors and metastasis. In support of this idea, suppressing NADK in MCF-10A cells, a breast epithelial cell line with no metastatic ability, has no effect in their ability to grow in 3D (Fig. S2g) while causing extensive growth defects in the highly metastatic 4T1 and LM2 cells (Fig. 2e and f, Figs. S2a and b). Together, our data reveal a critical role for NADK and the concomitant expansion of the total NADP(H) pools specifically in the progression of breast cancer into metastatic disease.

2.4. NADK does not promote metastasis through regulation of epithelial-to-mesenchymal transition (EMT)

EMT, an evolutionarily conserved developmental program, is one of the major drivers of metastatic ability [27–29]. Considering the intertwines of metabolism and EMT [30,31], we reasoned that NADK's ability to enable breast cancer metastasis could be related to EMT. To evaluate if this is the case, we suppressed NADK in the highly metastatic LM2 and 4T1 cells and evaluated the presence of epithelial and mesenchymal markers. Evaluation of the bona-fide mesenchymal markers fibronectin and vimentin as well as the extracellular matrix remodeller PAI-1 (serpine 1), a factor associated with EMT and metastasis [32], showed that NADK suppression does not reduce mesenchymal markers nor does it alter the expression of the canonical epithelial marker E-cadherin (Figs. S3a and b). To further explore a role for EMT in NADK's ability to regulate metastasis formation, we evaluated if suppressing NADK in MCF-10A cells (a widely used model for EMT studies) would block the ability of canonical inducers of EMT, such as TGFβ and TNFα [33]. Similarly to what we observed in LM2 and 4T1 cells, no clear effect of NADK suppression was detected in the expression of epithelial or mesenchymal markers (Fig. S3c). Together these data point for a role of NADK in powering metastasis formation in breast cancer independently of EMT and the epithelial/mesenchymal identity of the cancer cells.

2.5. NADK regulates redox balance and lipid synthesis in breast cancer metastasis

NADPH is the universal electron donor in reductive biosynthesis and detoxification of the cell [21]. To establish if the increase in NADK and consequent expansion of the $NADP^+$ pools affect metastatic ability by enabling ROS detoxification, we first measured ROS in 4T1 and LM2 cells upon NADK suppression. NADK knockdown in both cell lines resulted in suppression of antioxidant defences as shown by an expected decline in NADPH (Fig. 3a, Fig. S4a) as well as a pronounced decline in reduced glutathione levels, which relies on the reducing power of NADPH to be recycled (Fig. 3b, Fig. S4b). Accordingly, we observed a general, albeit variable, increase in ROS (Fig. 3c, Figs. S4c and d). ROS levels are notoriously dynamic and compartmentalized, making their steady-state detection challenging. To corroborate the effects of NADK suppression on ROS homeostasis we evaluated the redox status of peroxiredoxins, a family of cysteine-dependent enzymes that play a dominant role in the detoxification of hydrogen peroxide [34] and whose redox status is often used as a surrogate for ROS levels. Consistent with an increase in ROS, we observed a robust increase in the oxidation status of the cytosol as well as the mitochondria as evidenced by an increase in the oxidized fraction of peroxiredoxin 1 (PRDX1, cytosolic) and peroxiredoxin 3 (PRDX3, mitochondrial) upon NADK suppression (Fig. 3d). In addition to its importance in ROS detoxification, NADPH also powers reductive biosynthesis and plays a critical role in nucleotide and lipid synthesis. In line with the importance of NADPH levels to power fatty

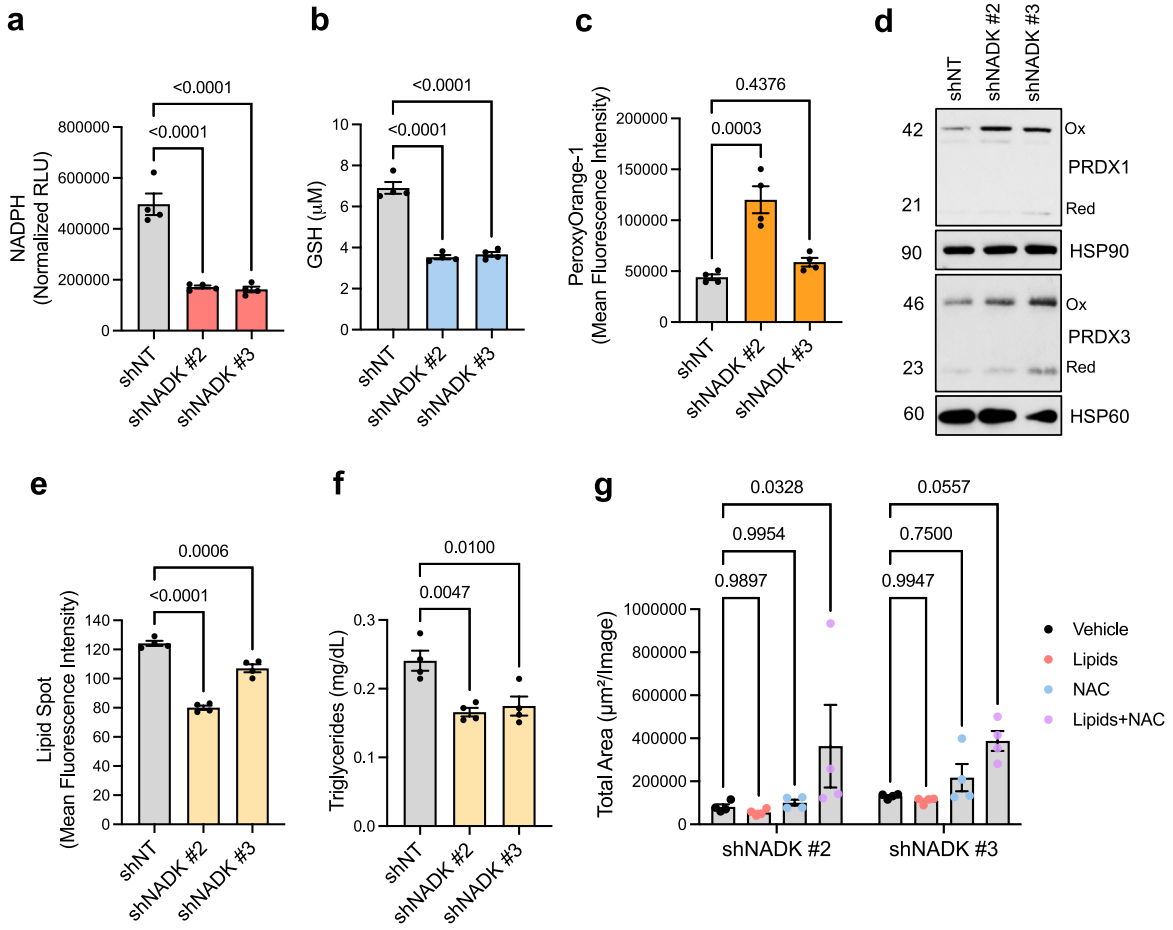

Fig. 3. NADK increases NADP(H) pools to sustain redox and anabolic reactions, and enables metastatic outgrowth. a, b, NADPH **(a)** and glutathione **(b)** levels in LM2 with NADK knockdown for 3 days (n = 4). **c,** H_2O_2 levels in LM2 with NADK knockdown for 3 days (n = 4). **d,** Redox status of PRDX1 and PRDX3 evaluated by immunoblot; representative image (n = 4). **e, f,** Neutral lipid **(e)** and triglyceride levels **(f)** in LM2 with NADK knockdown for 3 days (n = 4). **g,** Basal membrane extract 3D growth of LM2 cells with NADK knockdown supplemented with lipids, N-acetylcysteine (NAC) or the combination (n = 4). All values are expressed as mean ± SEM.

acid synthesis we observed a decline in intracellular lipid levels upon NADK suppression (Fig. 3e and f). However, NADK knockdown had no consistent effect on nucleotide levels, another biosynthetic pathway that relies on NADPH reducing power (Figs. S4e and f). Importantly, NAD^+ levels were not consistently altered upon NADK knockdown, suggesting that a potential effect of NADK in powering metastasis through regulation of NAD^+ levels is unlikely (Figs. S1e and f). Having shown that NADK activity powers ROS detoxification and lipid synthesis in metastatic breast cancer cells, we sought to determine if deregulation of these pathways is at the root of the decline in metastatic ability upon NADK silencing. Supplementation with either lipids or a powerful antioxidant (N-acetylcysteine – NAC) alone were not sufficient to rescue the defect in BME growth elicited by the knockdown of NADK (Fig. 3g, Fig. S4g). However, supplementation with both lipids and NAC gave 4T1 and LM2 cells with NADK suppression a growth advantage (Fig. 3g, Fig. S4g). Together, these observations suggest that expansion of the NADP(H) pools via *de novo* synthesis of $NADP^+$ by NADK is an important feature for successful metastasis of breast cancer, by increasing redox power to fuel antioxidant defences and lipid synthesis.

2.6. *NADK induction is regulated by H3.3 incorporation into chromatin in response to metastatic signals*

Next, we sought to understand how NADK is regulated during tumour progression. NADK's regulation is best known to occur via phosphorylation by the AGC kinases AKT [35] and PKC [25]. Thus, we reasoned that AKT and/or PKC activity might be the regulatory node that enables NADK's activity to power the expansion of NADP(H) pools necessary for progression into metastasis. Treatments of LM2 and 4T1 cells with an AKT, PKC or the combination of AKT and PKC inhibitors, while having the expected effect of blocking AKT and PKC activity, did not affect the NADP(H) pools of either cell lines (Figs. S5a–f). Further supporting a mechanism of NADK regulation by metastatic signalling independent of AKT and/or PKC, treatment with their inhibitors had no effect in the ability of LM2 cells to grow in 3D. In 4T1 cells PKC inhibition had no effect in their ability to grow in 3D (Fig. S5g), while AKT inhibition and the combination of AKT and PKC inhibition significantly reduced their ability to grow in 3D (Fig. S5h). However, AKT inhibition had no effect in the NADP(H) pools in 4T1, suggesting that the effect of AKT inhibition on 4T1's 3D growth is independent of its ability to regulate NADK and likely to be a consequence of the oncogenic hyperactivation of PI3K signalling characteristic of these cells [36].

Considering the importance of NADP(H) pools for redox control and anabolic processes, we reasoned that NADK induction might be an early event in the progression of breast cancers. To test this, we treated MCF10A cells with the well-established metastatic inducers TGFβ and TNFα [33]. Consistent with their ability to promote EMT and the acquisition of metastatic traits [33], three days of TGFβ/TNFα treatment was sufficient to increase the levels of $NADP^+$ in MCF10A cells (Fig. 4a). Moreover, TGFβ/TNFα treatment of HCC1806, a breast cancer cell line derived from a primary tumour, increased *de novo* production of $NADP^+$ from NAD^+ (Fig. 4b, Fig. S6a). Our initial observations suggest that in addition to NADK activity, NADK levels are upregulated in metastasis (Fig. 1), suggesting that the mechanism of *de novo* NADP(H) synthesis regulation in metastasis might lie on regulation of NADK levels. Accordingly, we observed that NADK levels were upregulated in MCF-10A, HCC1806 as well as in HCC38, another breast cancer cell line derived from a primary tumor, upon treatment with TGFβ/TNFα (Fig. 4c). To the best of our knowledge, no regulator of NADK levels has been described to date. However, we previously demonstrated that in order for breast cancer cells to acquire metastatic-like properties in response to TGFβ/TNFα, an epigenetic reprogramming regulated by histone H3 chaperones and the non-canonical H3.3 variant needs to occur [37]. Analysis of publicly available H3.3 chromatin immunoprecipitation sequencing (ChIP-seq) data in LM2 cells [37] demonstrated that H3.3 is deposited at the promoter region of NADK (Fig. 4d), suggesting that NADK regulation by metastatic signals such as TGFβ and TNFα might be mediated by H3.3 deposition and consequent transcriptional activation. In support of this hypothesis, ChIP-PCR analysis demonstrated H3.3 incorporation into the *NADK* promoter was elevated in response to TGFβ/TNFα treatment (Fig. 4e). H3.3 is thought to gap fill the DNA in response to stimuli that decrease the incorporation of canonical histones into chromatin [38]. Suppression of CAF-1, the histone chaperone complex in charge of depositing canonical histones into chromatin, was previously shown to be sufficient to trigger this H3.3 gap filling mechanism in breast cancer [37]. Thus, we reasoned that if H3.3 gap filling is mediating the NADK's increase in response to metastatic signals, suppression of the CAF-1 complex alone should mirror their

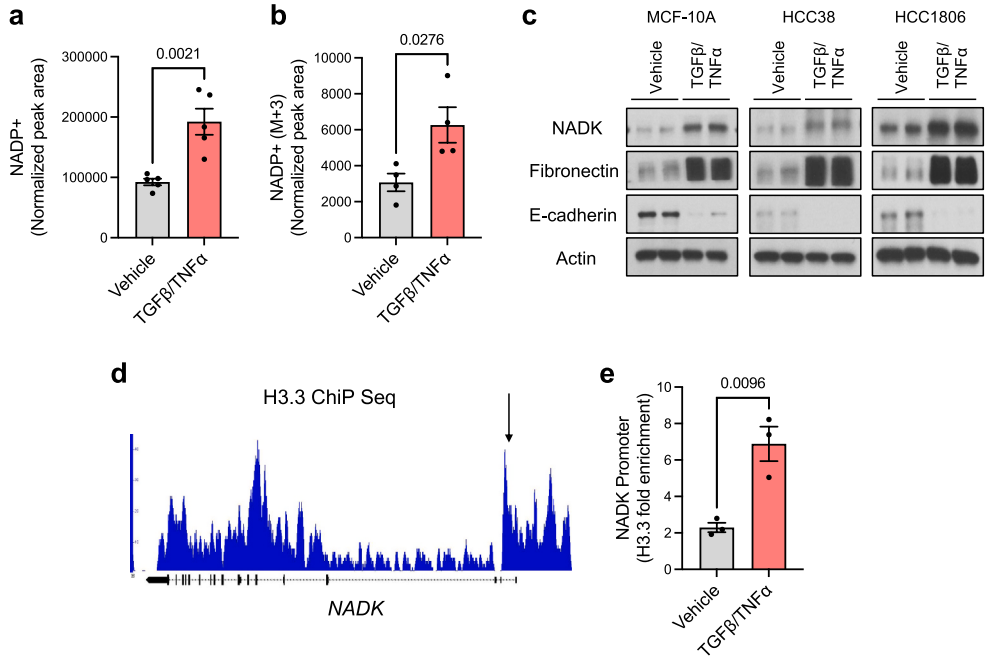

Fig. 4. Pro-metastatic signals drive *de novo* NAD^+ production and NADK induction. a, $NADP^+$ levels in MCF-10A cells treated with TGFβ + TNFα for 3 days (n = 5). **b,** *De novo* $NADP^+$ production from labelled NAM in HCC1806 cells treated with TGFβ + TNFα for 3 days (n = 4). **c,** NADK immunoblot in MCF-10A, HCC38 and HCC1806 cells treated with TGFβ + TNFα for 5 days; representative images (n = 4). **d,** H3.3 signal track of H3.3 ChIP-seq analysis in LM2 cells. **e,** H3.3 enrichment at the *NADK* promoter in MCF-10A treated with TGFβ + TNFα for 3 days; fold enrichment was determined using immunoglobulin G (IgG) as a control for the ChIP (n = 3).

effects on NADK. Suppressing the CAF-1 complex via shRNA-mediated silencing of its subunit CHAF1B resulted in a similar increase in H3.3 enrichment at the promoter of NADK, increased levels of NADK and concomitantly increased NADP(H) levels in non-metastatic breast cancer cells (Fig. 5a–d, Figs. S6b–d), mirroring the effects of TGFβ/TNFα treatments. Interestingly, while NADK levels are increased in HCC38 cells upon the suppression of the CAF-1 complex, there is an apparent discordance between the magnitude of the effect on NADK levels and the effects elicited on the NADP(H) pools (Figs. S6b–d), suggesting that another layer of NADP(H) pools regulation may be at play in this cell line.

Histone H3.3 deposition onto chromatin at genic regions is mediated by the histone chaperone, HIRA [39]. HIRA is known to become upregulated in conditions that trigger H3.3 gap filling of chromatin, including upon treatment with metastasis inducers [37]. In line with these previous findings, we observed that HIRA was induced both in

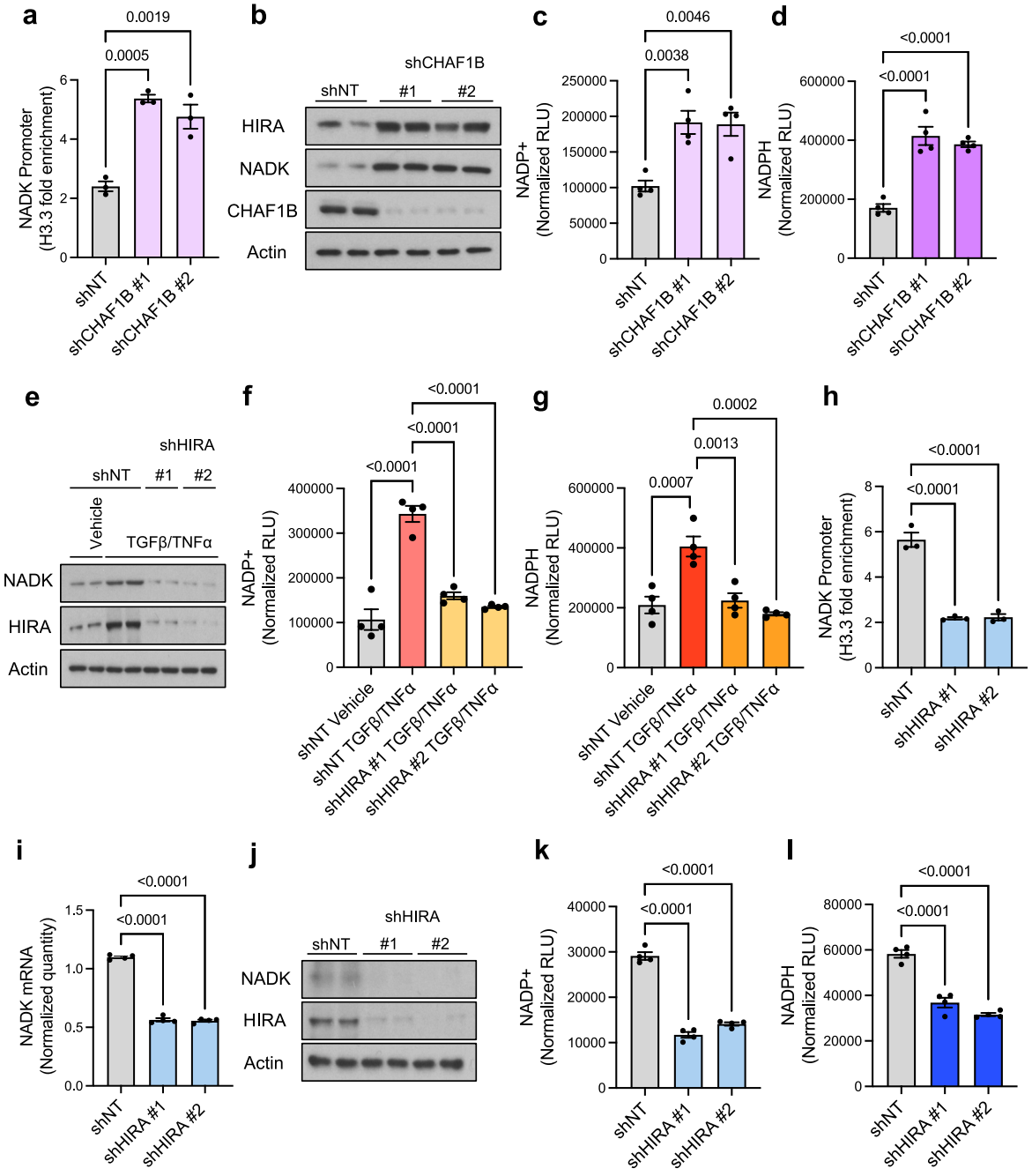

Fig. 5. H3.3 incorporation into chromatin in response to metastatic signalling drives NADK expression in breast cancer. a, H3.3 enrichment at the *NADK* promoter in MCF-10A cells with CHAF1B suppression for 3 days; fold enrichment was determined using immunoglobulin G (IgG) as a control for the ChIP (n = 3). **c,** NADK immunoblot in HCC1806 cells with CHAF1B suppression for 3 days; representative images (n = 4). **c, d,** $NADP^+$ **(c)** and NADPH **(d)** levels in HCC1806 cells with CHAF1B knockdown for 3 days (n = 4). **e,** NADK immunoblot in HCC1806 cells with HIRA knockdown treated with TGFβ + TNFα for 5 days; representative image (n = 4). **f, g,** $NADP^+$ **(f)** and NADPH **(g)** levels in HCC1806 cells with HIRA knockdown treated with TGFβ + TNFα for 5 days (n = 4). **h,** H3.3 enrichment at the *NADK* promoter in LM2 cells with HIRA knockdown for 3 days; fold enrichment was determined using immunoglobulin G (IgG) as a control for the ChIP (n = 3). **i,** NADK mRNA quantity in LM2 cells with HIRA knockdown for 3 days (n = 4). **j,** NADK immunoblot in LM2 cells with HIRA knockdown for 3 days; representative image (n = 4). **k, l,** $NADP^+$ **(k)** and NADPH **(l)** levels in LM2 cells with HIRA knockdown for 3 days (n = 4). All values are expressed as mean ± SEM.

response to artificially triggering H3.3 gap filling through CAF-1 direct suppression (Fig. 5b, Fig. S6b) as well as upon treatment with TGFβ/TNFα (Fig. 5e, Fig. S6e), mirroring the effects these perturbations elicit on NADK levels (Fig. 5b and e, Figs. S6b and e). Suppression of HIRA ablated the ability of TGFβ and TNFα to induce NADK levels and to increase NADP(H) levels in HCC1806 and HCC38 cells (Fig. 5e–g, Figs. S6e–g), suggesting that HIRA is the mechanistic link between histone H3.3 deposition and NADK regulation. Finally, because NADK levels are elevated in metastatic breast cancer cells (Fig. 1i–k) and H3.3 was found to be deposited at the NADK promoter in the highly metastatic LM2 cells (Fig. 4d), we evaluated if suppressing HIRA in this context would also affect NADK levels and the NADP(H) pools. Our data showed that suppression of HIRA in LM2 cells as well as in another human breast cancer cell line with high metastatic ability, Hs578T, decreased H3.3 enrichment at the NADK promoter, resulting in a decrease in NADK mRNA and protein levels and ultimately led to the contraction of NADP(H) pools in these cells (Fig. 5h-l, Figs. S6h–k). These data show that metastatic signals drive NADK expression through deposition of H3.3 into the NADK promoter resulting in its activation, illustrating an epigenetic mechanism that regulates the NADP(H) pools and is relevant for human breast cancer disease.

3. Conclusion

Late-stage metastatic breast cancer remains a fatal diagnosis. Breast cancer metastases are highly resistant to therapy and account for more than 90% of breast cancer mortality. Thus, identification of factors that are essential for breast cancer metastasis and consequently may constitute important therapeutic targets is essential to our ability to effectively treat late-stage metastatic breast cancer. Here, we present evidence for NADK upregulation as an essential metabolic adaptation of breast cancer metastasis. During the metastatic cascade, NADK levels increase in breast cancer cells leading to expansion of their NADP(H) pools, which power anabolic reactions and antioxidant systems to enable metastases to arise and thrive. Together these results put forward NADK as an important new and druggable therapeutic target for advanced breast cancers and metastatic disease.

Mechanistically, we demonstrated that NADK upregulation occurs in response to metastatic signals, such as TGFβ and TNFα, as part of a chromatin remodelling program that impinges on the histone H3.3 variant [37]. Although more in-depth studies are necessary to fully determine the scope of H3.3-mediated regulation of metabolic and redox pathways in breast cancer metastasis and other types of cancer, this study reveals a previously unknown role of H3.3 in regulation of redox and metabolic pathways. Moreover, these findings lay the foundation for a dynamic relationship between metabolism and nucleosome remodelling mediated by differential incorporation of the histone variants, with potential implications for regulation of cell fate decisions and consequently physiological and pathological responses.

4. Materials and methods

4.1. Cell lines

HCC38, HCC1806, BT20, MDA-MB-231, Hs578T and MCF10A cells were obtained from American Type Culture Collection (ATCC). 4T1 and 4T07 mouse breast cancer cell line clones were originally derived by Dr. F. Miller [19] and obtained from Dr. William Schiemann. MDA-MB-231 LM2 (referred to as LM2) subclone [18] was obtained from Dr. Massague's lab. HEK293T cells were obtained from GenHunter. All cell lines were maintained at 37 °C and 5% CO_2 in the presence of 100 unit/mL penicillin and 100 μg/mL streptomycin (Gibco) and were routinely tested for mycoplasma using MycoAlert mycoplasma detection kit (Lonza). HCC38, HCC1806, BT20, MDA-MB-231, 4T1 and 4T07 cells were cultured in RPMI-1640 medium supplemented with 10% FBS. Hs578T cells were maintained in high glucose DMEM with 0.01 mg/mL insulin and 10% FBS, while LM2 and HEK293T cells were cultured in high glucose DMEM with 10% FBS. MCF10A cells were maintained in DMEM:F12 media supplemented with 5% horse serum (Gibco), 10 μg/mL insulin (Sigma-Aldrich), 100 ng/mL cholera toxin (Sigma-Aldrich), 20 ng/mL EGF (Peprotech), and 0.5 mg/mL hydrocortisone (Sigma-Aldrich). The cells used for the experiments in this manuscript always tested negative for mycoplasma.

4.2. Cell culture treatments

Some cells were treated with 5 ng/mL of recombinant human TGFβ (PeproTech) and 5 ng/mL of recombinant human TNFα (PeproTech) as metastatic inducers for the indicated time periods. When cells with genetic suppression of a gene of interest were also treated with TGFβ1 and TNFα, the cells were transduced and selected as described below and then treated with 5 ng/mL of recombinant human TGFβ (PeproTech) and 5 ng/mL of recombinant human TNFα (PeproTech).

4.3. 3D soft Agar colony formation assay

As the bottom layer a coating of 1:1 ratio of 2 x DMEM (Millipore): 1.2% SeaPlaque Agarose (Lonza) was applied to 6-well plates, and allowed to set overnight. The top layer was applied the next day (1:1 ratio of 2 x DMEM and 0.7% agarose) containing 5000 of the indicated cells per well. The next day 0.5 mL 1 x DMEM with selection antibiotic was added to each well. The media was changed once a week and the colonies were allowed to grow for 4–6 weeks. To visualize and quantify 3D colonies, cells were stained in 0.005% Crystal violet/10% Ethanol aqueous solution for 3 h, and de-stained in water overnight. Colonies were counted by eye.

4.4. Basal membrane extract (BME) 3D growth assay

96-well plates were coated with 40 μL of growth-factor reduced BME (Cultrex), and plates were allowed to set for at least an hour at 37 °C. 2000 cells/well in 100 μL media supplemented with 2% FBS, 2% BME and appropriate selection antibiotics was layered on top of the BME coating. The plates were imaged with Incucyte Live Imaging system every 12 h. The cells were fed fresh media supplemented with 2% FBS every 4 days. Where indicated, cells were also treated with 0.5 μM MK-2206 (hydrochloride) (Akt inhibitor, 1032350-13-2, Cayman Chemical), 0.2 μM Sotrastaurin (PKC inhibitor, 425637-18-9, Cayman Chemical) or its combination. Where indicated cell media was also supplemented with 2 mM N-acetyl-L-cysteine (NAC, Sigma-Aldrich), or lipids (12 μg/mL low density lipoprotein (Kalen Biomedical) and 50 μM oleate (Sigma-Aldrich)) or in combination. Colony growth was analysed using Incucyte software (v. 2021A) as total area covered by the colonies.

4.5. Isotope tracing of de novo $NADP^+$ generation

Cells were grown in nicotinamide (NAM) free media with 10% dialyzed serum (Sigma-Aldrich) to 60–80% confluency in 6 cm plates. Prior to harvesting cells were treated with 32 μM [2,4,5,6-^{2}H]NAM for 2 h. The media was aspirated and 1 mL of ice-cold 40% MeOH/40% acetonitrile/20% water/0.5% formic acid mixture was added to the plates and incubated for 30 s before 80 μL of 2 M NH_4HCO_3 was added to neutralize [40]. Plates were moved to −20 °C for 30 min, before cells were scraped off and moved into microcentrifuge tubes. The tubes were incubated on dry ice for 5 min centrifuged at 16,000 g for 10 min at 4 °C. Supernatants were collected and frozen at −80 °C until further processing. Within 24 h before analysis by liquid chromatography coupled to a mass spectrometer (LC-MS), the supernatants were centrifuged again at 16,000 g for 20 min to remove any debris. The LC–MS method was based on hydrophilic interaction chromatography (HILIC) coupled to the Q Exactive PLUS mass spectrometer (Thermo Scientific). The LC separation was performed on a XBridge BEH Amide column (2.1 × 150

mm, 3.5 μm particle size, Waters, Milford, MA). Solvent A is 95%: 5% H2O: acetonitrile with 20 mM ammonium bicarbonate, and solvent B is acetonitrile. The gradient was 0 min, 85% B; 2 min, 85% B; 3 min, 80% B; 5 min, 80% B; 6 min, 75% B; 7 min, 75% B; 8 min, 70% B; 9 min, 70% B; 10 min, 50% B; 12 min, 50% B; 13 min, 25% B; 16 min, 25% B; 18 min, 0% B; 23 min, 0% B; 24 min, 85% B; 30 min, 85% B. The following parameters were maintained during the LC analysis: flow rate 150 mL/min, column temperature 25 °C, injection volume 10 μL and autosampler temperature was 5 °C. For the detection of metabolites, the mass spectrometer was operated in both negative and positive ion mode. The following parameters were maintained during the MS analysis: resolution of 140,000 at *m/z* 200, automatic gain control (AGC) target at 3e6, maximum injection time of 30 ms and scan range of *m/z* 75–1000. If variation in cell numbers was observed between conditions, the data were normalized to the protein content. The EL-MAVEN software version 12 was used to analyze the data, and natural 2H abundance was taken into account to correct all labeling patterns using AccuCor [41]. When normalization was required due to variation in cell number in between samples, the original data were normalized to protein content.

4.6. NAD^+ and NADP(H) measurement

Whenever data are presented as normalized peak area, cells grown normally without any tracers were harvested and analysed through LC-MS as described above in the isotope tracing section to determine the NAD^+ or NADP(H) levels in the cells. Whenever data are presented as relative light unit (RLU), NADP/NADPH-Glo™ Assay (Promega), a luminescence-based method, was used to measure $NADP^+$ and NADPH of 100,000 cells on 96-well assays according to manufacturer's instructions. The luminescence was measured using a Varioskan microplate reader (Thermo Scientific). Primary tumor samples and metastatic foci were mechanically homogenized and lysed for 1 h in 1% DTAB lysis buffer prior analysis.

4.7. Nucleotide measurements

Polar metabolites were extracted from the indicated cell lines using 80% (v/v) aqueous methanol as described before [42]. Targeted liquid chromatography-tandem mass spectrometry (LC-MS/MS) was performed using a 5500 QTRAP triple quadrupole mass spectrometer (AB/SCIEX) coupled to a Prominence UFLC HPLC system (Shimadzu) with Amide HILIC chromatography (Waters). Data were acquired in selected reaction monitoring (SRM) mode using positive/negative ion polarity switching for steady-state polar profiling of greater than 260 molecules. Peak areas from the total ion current for each metabolite SRM transition were integrated using MultiQuant v2.0 software (AB/SCIEX).

4.8. Generation of stable cell lines

For gene silencing experiments, shNT (shGFP—TRCN0000072181), shNADK#1 (TRCN0000037700), shNADK#2 (TRCN0000199808), shNADK#3 (TRCN0000199040), shNadk#1 (TRCN0000297518), shNadk#2 (TRCN0000278616), shCHAF1B #1 (TRCN0000074279), shCHAF1B #2 (TRCN0000074278) were obtained from Sigma, and shHIRA #1 (TRCN0000020514) and shHIRA #2 (TRCN0000020515) were obtained from OpenBiosystems. For stable overexpressing cell lines a pSMPUW-IRES-Hygro lentiviral vector encoding the full sequence of human NADK (a gift from Dr. Gerta Hoxhaj and described before [35] was used. pMD2.G (Addgene plasmid 12259) and psPAX2 (Addgene plasmid 12260) constructs were co-transfected with each construct in HEK293T cells using X-tremeGENE HP (Roche) according to manufacturer's protocols to produced viral particles expressing the shRNA of interest. The media was refreshed 24 h after transfection and media containing virus was collected 72 h after transfection. Filtered virus was used for transductions in the presence of 8 μg/mL polybrene (Sigma-Aldrich). Cells were selected with 2 μg/mL puromycin (Sigma-Aldrich) starting 24 h after transduction, and 2 μg/mL puromycin (Sigma-Aldrich) was maintained in their growth media for the duration of the experiments. TPNOX and the control GFP cDNAs were custom made and purchased from VectorBuilder (C-terminally FLAG-tagged lentiviral constructs under EF1a promoter)., pRSV-Rev (Addgene plasmid 12253), pMDLg/pRRE (Addgene plasmid 12251) and pMD2.G (Addgene plasmid 12259) co-transfected with each construct in HEK293T cells using X-tremeGENE HP (Roche) according to manufacturer's protocols to produced viral particles expressing the cDNAs of interest. The media was refreshed 24 h after transfection and media containing virus was collected 72 h after transfection. Filtered virus was used for transduction of 4T1 cells in the presence of 8 μg/mL polybrene (Sigma-Aldrich). 4T1 cells were selected with 5 μg/mL of Blasticidin·HCl (Thermo Fisher) starting 24 h after transduction, and 5 μg/mL of Blasticidin·HCl (Thermo Fisher) was maintained in their growth media for the duration of the experiments.

4.9. Immunoblots for total cell lysates

Proteins were harvested with 10% TCA solution (10% trichloroacetic acid, 25 mM NH_4OAc, 1 mM EDTA, 10 mM Tris·HCl pH 8.0), and pelleted proteins were resolubilized in a 0.1 M Tris·HCl pH 11 solution containing 3% SDS by boiling for 10–15 min. Protein concentration was determined with DC Protein Assay kit II (BioRad)and 20 μg total protein per sample was run on SDS-PAGE under reducing conditions, and then transferred from the gels to nitrocellulose membranes (GE Healthcare) electrophoretically. The membranes were blocked in 5% milk and then incubated with the primary antibodies overnight at 4 °C. The antibodies used to detect the proteins of interest were: E-Cadherin (610181 - BD Biosciences, Dilution 1:1000), Fibronectin (ab2413 – Abcam, Dilution 1:5000), NADK (55948S - Cell Signaling, Dilution 1:500), CHAF1B (HPA021679 – Sigma-Aldrich, Dilution 1:1000), HIRA (ab129169 – Abcam, Dilution 1:500), Akt (2966S – Cell Signaling, 1:1000), Phospho-Akt Ser473 (4060S – Cell Signaling, 1:1000), Phospho-MARCKS (Ser159/163) (11992S - Cell Signaling Technology, Dilution 1:500), MARCKS (5607S - Cell Signaling Technology, Dilution 1:1000), PAI-1 (612024 - BD Biosciences, Dilution 1:500), Vimentin (5741S - Cell Signaling Technology, Dilution 1:1000), Vinculin (V9264 – Sigma-Aldrich, Dilution 1:10,000) and Actin (sc1615 - Santa Cruz, Dilution 1:10,000). The membranes were then incubated with the appropriate horseradish peroxidase–conjugated (HRP) anti-rabbit (NA934-Cytiva, Dilution 1:10,000), anti-mouse (NA931-Cytiva, Dilution 1:10,000), or anti-goat (AP180P-Millipore, Dilution 1:10,000) immunoglobulin for 2 h at room temperature. Amersham ECL detection system (GE Healthcare) was utilized to develop the signals.

4.10. Redox immunoblotting

PRDX1 and PRDX3 oxidation states were assessed in accordance with a previously established protocol [43]. For each biological replicate, 500,000 cells were seeded overnight on a 6-well plate. Cells were then washed twice with cold PBS (Hyclone) and overlaid with 200 μL of alkylation buffer (40 mM HEPES [VWR], 50 mM NaCl [Fisher Scientific], 1 mM EGTA [VWR], Pierce Protease Inhibitor [Fisher Scientific]) supplemented with 200 mM N-ethylmaleimide (NEM; Alfa Aesar). Cells were incubated for 10 min at room temperature and then 20 μL of 10% CHAPS detergent was added and cells incubated at room temperature for an additional 10 min to lyse cells. Lysates were then collected, vortexed, and cleared by centrifugation for 15 min at 17,000 g at 4 °C. Supernatants were isolated to quantify protein and 5–10 μg protein samples were mixed with a 4X non-reducing buffer prior to separation by SDS-PAGE. Separated proteins were transferred to a nitrocellulose membrane and incubated with antibodies recognizing HSP60 (Cell Signaling Technologies, D307), HSP90 (Cell Signaling Technologies, 4874S), PRDX1 (Cell Signaling Technologies, D5G12), or PRDX3

(Abcam, ab73349). HRP-conjugated secondary antibodies and enhanced chemiluminescence were used for redox immunoblotting.

4.11. NADK fluorescent immunohistochemistry (IHC)

Immunostaining for NADK was performed on paraffin-embedded FFPE tumor tissue sections (TMA slide, Serial #BR10010f; US Biomax). The slide was melted at 70 °C for 30 min and was further deparaffinized using xylene and rehydrated in serial alcohol washes. The slide was pressure cooked at 15 PSI for 15 min in a 1X DAKO antigen retrieval buffer (Agilent Technologies). Tissue sections were subject to two 5-min standing washes in PBS prior to blocking in 1X Carb-Free Blocking Solution (Vector Labs) for 3 h at room temperature. The slide was next washed twice and incubated with anti-NADK primary antibody (15548-1-AP dilution:1:50; Proteintech) overnight at 40 °C. Next day, the slide was washed with PBS three times and incubated with Alexa-Fluor 647 (Cy5) anti-rabbit secondary antibody (A32733 dilution:1/250; Invitrogen) and eFluor 570 (Cy3) Anti-Pan Cytokeratin (41-9003-82 dilution:1/400; Invitrogen) in dark for 3 h at room temperature. The slide was next washed and mounted with Vectashield + DAPI (Vector Laboratories). TMA was scanned on the Aperio FL (Leica Biosystems) using DAPI, Cy3 and Cy5 fluorescent filters and the whole slide FL image scan was loaded into HALO Image Analysis Platform v3.3 (Indica Labs, Albuquerque, NM) for quantitative image analysis. The TMA was segmented in HALO and each core is reviewed for lifted and blurred areas of tissue and an inclusion or exclusion for analysis annotations are created. A random forest machine learning classifier was trained on multiple tissue cores using the PCK and DAPI channels to identify tumor vs non-tumor tissue. The tissue is then segmented into individual cells using the DAPI marker which stains cell nuclei. For each marker, a positivity threshold within the nucleus or cytoplasm are determined per marker based on visual FL staining. After setting a positive fluorescent threshold for each staining marker, the slide is analysed with the algorithm. The generated data includes positive cell counts for each fluorescent marker and percent of cells positive for the marker. Along with the summary output, a per-cell analysis can be exported to provide the marker status and fluorescent intensities of every individual cell within an image.

4.12. Gene expression analysis

Total RNA was extracted from cells grown on 6 cm dishes until 70–80% confluency using the PureLink RNA isolation kit (Life Technologies). To digest contaminating DNA, isolated RNA was treated with DNAse I (Amplification grade, Sigma-Aldrich). cDNA was synthesized with iSCRIPT cDNA synthesis kit (BioRad) and quantitative PCR (qPCR) using SYBR green master mix (Life Technologies) was performed on a QuantStudio6 Real-Time PCR system (Life Technologies, software version v1.3). Tata Binding Protein (TBP) expression were used to normalize NADK expression levels. The primer sequences are.

TBP_forward: GAGCCAAGAGTGAAGAACAGTC;
TBP_reverse: GCTCCCCACCATATTCTGAATCT;
NADK_forward: GAAGCAAGGAACACAGCATG;
NADK_reverse: CTCTCAAACCAGTCGCTCAC

4.13. Lung colonization in mice

Female nu/nu athymic mice, 4 to 6 weeks old, were obtained from Envigo. The animals were allowed acclimate for at least 7 days before experiments. The mice were maintained at Weill Cornell Medicine vivarium under standard husbandry conditions with unrestricted access to food and water in compliance with the Weill Cornell Medicine Institutional Animal Care and Use Committee (IACUC) protocols. The animal room was maintained with a 12 h light-dark cycle at 21–23 °C, around 50% humidity and. The standard chow, PicoLab Rodent Diet 5053 (Labdiet, Purina) containing 20% protein and 5% fat, was used. The maximum tumor size allowed—20 mm or 2.5 cm^3, or 10% of the animal's body weight—by the IACUC protocol was not exceeded.

Female nu/nu athymic mice were injected intravenously (tail-vein) with 100,000 LM2 cells with knockdown of NADK. For each experimental group 10 mice were used. IVIS Spectrum CT Pre-Clinical In Vivo Imaging System (PerkinElmer) was used to monitor the metastases to evaluate lung colonization. The luminescence was quantified 6 weeks after the injections using the Living Image Software (v4.5, PerkinElmer). The Weill Cornell Medicine IACUC guidelines were followed during the experiments.

4.14. Spontaneous metastasis in mice

Female BALB/c (BALB/cAnNCrl) mice were injected orthotopically into both 4th mammary glands with 5000 4T1 cells with or without NADK knockdown. Tumors from both sides were surgically removed 3 weeks after inoculation. Mice were sacrificed 3 weeks after tumor removal. Lung colonization was determined using Bouin's yellow stain fixative (Millipore Sigma) and counting of lung surface metastatic foci. Primary tumors as well as metastatic nodules were collected and flash-frozen for subsequent *in vitro* analysis. Primary tumor size was measured weekly using caliper. Mice were administered with analgesics for a period of 5 days after each surgery to reduce pain.

4.15. Flow cytometry analyses of ROS

For all analyses of ROS, 500,000 cells of each biological replicate were seeded overnight on a 6-well plate. Total cellular ROS levels were determined with the fluorescent dye, CellRox Deep Red (Invitrogen), according to the manufacturer's protocol. Briefly, cells were incubated in 1 mL of fresh media for 4 h, at which point 2 μL of 2.5 mM CellROX Deep Red was added to each well for a final concentration of 5 μM. Cells were incubated with CellROX Deep Red for 30 min and then collected for analysis. Cellular H_2O_2 levels were determined using the fluorescent dye, Peroxy Orange-1 (Fisher Scientific). Cells were incubated in 1 mL of fresh media for 4 h, then washed twice with PBS (Hyclone) and incubated in 1 mL of 5 μM Peroxy Orange-1 for 40 min. The fluorescence of dye-loaded cells was determined by flow cytometry with a BD Accuri C6 Plus Flow Cytometer (BD Biosciences). An allophycocyanin (APC) channel was used for analyses of CellROX Deep Red fluorescence, whereas a phycoerythrin (PE) channel was used for analyses of Peroxy Orange-1 fluorescence. The mean fluorescence intensity of 10,000 discrete events were calculated for each biological replicate.

4.16. GSH measurement

Cells were seeded and grown to 80% confluency on 96-well plates. Luminescence based GSH-Glo™ Assay (Promega) was used to determine the cellular glutathione (GSH) levels of 100,000 cells on 96-well according to the manufacturer's manual. The luminescence was measured using a Varioskan microplate reader (Thermo Scientific).

4.17. Lipid droplet stain

500,000 cells were seeded on 6-well plates overnight. Cells were incubated with LipidSpot™ 610 (Biotium) for 30 min at 37 °C to stain lipid droplets according to manufacturer's instructions. Samples were analysed by SONY SH800S flow cytometer (SONY). The fluorescence of LipidSpot™ 610 was determined using Texas Red channel (excitation/emission at ~592/638 nm). Acquired FCS files were exported and analysed using FlowJo software (v10.0.7; BD). Cell aggregates and debris were excluded from the analysis based on a dual-parameter dot plot in which the pulse ratio (signal height/y-axis vs. signal area/x-axis) was displayed. The median fluorescence intensity of 20,000 events were calculated for each biological replicate.

4.18. Triglyceride measurement

Cells were seeded on 6 cm dishes and grown to 80% confluency. Triglyceride Colorimetric Assay Kit (Cayman Chemical) was used to determine the triglyceride levels in cells according to the manufacturer's manual. The absorbance was measured using a Varioskan microplate reader (Thermo Scientific).

4.19. H3.3 signal tracks

ChIP-seq data for H3.3 in LM2 cells [37] (GEO: GSE120313) was used to visualize H3.3 signal tracks for the NADK gene using Integrated Genome Browser (IGB) [44].

4.20. ChIP-PCR

ChIP-IT Express (Active Motif) kit was used to perform chromatin immunoprecipitation (ChIP) according to the manufacturer's instructions. The chromatin was sheared enzymatically for 10 min (ChIP-IT Express Enzymatic Shearing Kit, Active Motif). Instead of the magnetic beads from the kit, Dynabeads (1:1 protein A to protein G; Life Technologies) were used. Anti-H3.3 (17–10245, Millipore) or anti-Rabbit IgG (sc-2027, Santa Cruz) antibodies were used for the immunoprecipitation. Chromatin IP DNA purification kit (Active Motif) was used to purify DNA and qPCR was performed with SYBR Green master mix (Life Technologies) on QuantStudio Pro 6 (Life Technologies) using the primer set for NADK listed below, corresponding to the DNA sequence on NADK promoter indicated with a red arrow on Fig. S3a.

NADK-ChIP-forward: CGCAGTTCCAACAAACACTAC:
NADK-ChIP-reverse: GAGGACTCGGGGAGTTGG

4.21. Statistical analysis

GraphPad Prism 7 or 9, and Microsoft Excel 2013 or 365 were utilized for data analyses. was used to determine significance When two conditions were compared two-tailed Student's *t*-test, and for experiments with more than two conditions ANOVA analyses were used to determine significance. Data are from at least three independent experiments and represented as the mean ± SEM (standard error of the mean) of individual data points. Number of replicates and animals are reported in the figure legends. Normal distribution of samples was not determined, but similar variances between groups were observed in all experiments.

Author's contributions

A.P.G conceived the project. D.I., S.D. and T.S. performed all the molecular biology experiments, the 3D growth-related experiments, the NADP(H) and GSH measurements, the mechanistic experiments, prepared cells for mass spectrometry and isotope tracing analysis and assisted on all other experiments. M.R.M. performed the mass spectrometry and isotope tracing analysis. N.P.W. performed the ROS measurements and the redox blots. S.D. performed the lipid analysis. V.L. performed the lung colonization experiment. S.D. and T.O. performed the spontaneous metastasis experiments. E.A. performed the NADK analysis in human breast cancer patient samples. A.P.G. performed the ChIP experiments. J.A. analysed nucleotide levels. A.P.G., M.R.M, G.M.D. and E.L-L. supervised the project. A.P.G., D.I., T.S., N.P.W., S.D., V.L., E.A. and M.R.M analysed the data. The manuscript was written by A.P.G. and edited by D.I., S.D., T.S., N.P.W., G.M.D and M.R.M. All authors discussed the results and approved the manuscript.

Funding

The Gomes Lab is supported by a Pathway to Independence Award to A.P.G. from NCI (R00CA218686), a New Innovator Award from OD/NIH (DP2AG0776980), an ACS scholar award (RSG-22-164-01-MM), internal funds from the Moffitt Cancer Center and grants from the American Lung Association, the Florida Health Department Bankhead-Coley Research Program (21B06), the Florida Breast Cancer Foundation, the Phi Beta Psi Sorority, and METAvivor. T.S. was supported by the NIH F31 pre-doctoral fellowship program (F31CA220750). S.D. is supported by a Miles for Moffitt Postdoctoral Fellowship. M.R.M is supported by the HHMI Hanna H. Gray Fellows Program Faculty Phase (Grant #GT15655). G.M.D. is supported by the NIH/NCI (R37CA230042). This work was also supported by Moffitt's Cancer Center Support Grant from NCI (P30CA076292) through the Analytic Microscopy Core. No potential conflicts of interest were disclosed by the authors.

Availability of data and materials

The raw data supporting the western blots can be found in the Supplementary data. The accession number for the raw ChIP-sequencing data that is previously published [37] and publicly available is GEO: GSE120313. These data were used to generate H3.3 tracks for the NADK gene. The remaining data that support the findings of this study are available from the corresponding author upon request.

Declaration of competing interest

The authors declare that they have no conflict of interest.

Data availability

Data will be made available on request.

Acknowledgements

We are grateful to Dr. John Blenis and members of the Gomes, DeNicola and Blenis Laboratories as well as Dr. Gerta Hoxhaj for critical input on this project. We are also thankful to Dr. William Schiemann for the 4T1 clones, Dr. Joan Massague for the MDA-MB-231 LM2 cells and Dr. Gerta Hoxhaj for the NADK overexpressing construct.

Appendix A. Supplementary data

Supplementary data to this article can be found online at https://doi.org/10.1016/j.redox.2023.102627.

References

[1] S. Valastyan, R.A. Weinberg, Tumor metastasis: molecular insights and evolving paradigms, Cell 147 (2) (2011) 275–292, https://doi.org/10.1016/j.cell.2011.09.024. PubMed PMID: 22000009; PMCID: PMC3261217.
[2] A.C. Chiang, J. Massague, Molecular basis of metastasis, N. Engl. J. Med. 359 (26) (2008) 2814–2823, https://doi.org/10.1056/NEJMra0805239. Epub 2008/12/26, PubMed PMID: 19109576; PMCID: PMC4189180.
[3] G.P. Gupta, J. Massague, Cancer metastasis: building a framework, Cell 127 (4) (2006) 679–695, https://doi.org/10.1016/j.cell.2006.11.001. Epub 2006/11/18, PubMed PMID: 17110329.
[4] M.G. Vander Heiden, L.C. Cantley, C.B. Thompson, Understanding the Warburg effect: the metabolic requirements of cell proliferation, Science 324 (5930) (2009) 1029–1033, https://doi.org/10.1126/science.1160809. PubMed PMID: 19460998; PMCID: PMC2849637.
[5] N.N. Pavlova, C.B. Thompson, The emerging hallmarks of cancer metabolism, Cell Metabol. 23 (1) (2016) 27–47, https://doi.org/10.1016/j.cmet.2015.12.006. PubMed PMID: 26771115; PMCID: PMC4715268.
[6] A. Zhu, D. Lee, H. Shim, Metabolic positron emission tomography imaging in cancer detection and therapy response, Semin. Oncol. 38 (1) (2011) 55–69, https://doi.org/10.1053/j.seminoncol.2010.11.012. PubMed PMID: 21362516; PMCID: PMC3075495.
[7] D. Hanahan, R.A. Weinberg, Hallmarks of cancer: the next generation, Cell 144 (5) (2011) 646–674, https://doi.org/10.1016/j.cell.2011.02.013. PubMed PMID: 21376230.
[8] C. Dong, T. Yuan, Y. Wu, Y. Wang, T.W. Fan, S. Miriyala, Y. Lin, J. Yao, J. Shi, T. Kang, P. Lorkiewicz, D. St Clair, M.C. Hung, B.M. Evers, B.P. Zhou, Loss of FBP1 by Snail-mediated repression provides metabolic advantages in basal-like breast

cancer, Cancer Cell 23 (3) (2013) 316–331, https://doi.org/10.1016/j.ccr.2013.01.022. PubMed PMID: 23453623; PMCID: PMC3703516.
[9] E. Piskounova, M. Agathocleous, M.M. Murphy, Z. Hu, S.E. Huddlestun, Z. Zhao, A. M. Leitch, T.M. Johnson, R.J. DeBerardinis, S.J. Morrison, Oxidative stress inhibits distant metastasis by human melanoma cells, Nature 527 (7577) (2015) 186–191, https://doi.org/10.1038/nature15726. Epub 2015/10/16, PubMed PMID: 26466563; PMCID: PMC4644103.
[10] Y.D. Shaul, E. Freinkman, W.C. Comb, J.R. Cantor, W.L. Tam, P. Thiru, D. Kim, N. Kanarek, M.E. Pacold, W.W. Chen, B. Bierie, R. Possemato, F. Reinhardt, R. A. Weinberg, M.B. Yaffe, D.M. Sabatini, Dihydropyrimidine accumulation is required for the epithelial-mesenchymal transition, Cell 158 (5) (2014) 1094–1109, https://doi.org/10.1016/j.cell.2014.07.032. PubMed PMID: 25171410; PMCID: PMC4250222.
[11] S. Drapela, A.P. Gomes, Metabolic requirements of the metastatic cascade, Curr. Opin. Struct. Biol. 28 (2021), https://doi.org/10.1016/j.coisb.2021.100381. Epub 2021/10/26, PubMed PMID: 34693082; PMCID: PMC8535854.
[12] G. Bergers, S.M. Fendt, The metabolism of cancer cells during metastasis, Nat. Rev. Cancer 21 (3) (2021) 162–180, https://doi.org/10.1038/s41568-020-00320-2. Epub 2021/01/20, PubMed PMID: 33462499; PMCID: PMC8733955.
[13] L.A. Broadfield, A.A. Pane, A. Talebi, J.V. Swinnen, S.M. Fendt, Lipid metabolism in cancer: new perspectives and emerging mechanisms, Dev. Cell 56 (10) (2021) 1363–1393, https://doi.org/10.1016/j.devcel.2021.04.013. Epub 2021/05/05, PubMed PMID: 33945792.
[14] J.G. Gill, E. Piskounova, S.J. Morrison, Cancer, oxidative stress, and metastasis, Cold Spring Harbor Symp. Quant. Biol. 81 (2016) 163–175, https://doi.org/10.1101/sqb.2016.81.030791. Epub 2017/01/14, PubMed PMID: 28082378.
[15] A. Tasdogan, J.M. Ubellacker, S.J. Morrison, Redox regulation in cancer cells during metastasis, Cancer Discov. 11 (11) (2021) 2682–2692, https://doi.org/10.1158/2159-8290.CD-21-0558. Epub 2021/10/16, PubMed PMID: 34649956; PMCID: PMC8563381.
[16] M. Martin-Perez, U. Urdiroz-Urricelqui, C. Bigas, S.A. Benitah, Lipid metabolism in metastasis and therapy, Curr. Opin. Struct. Biol. 28 (2021), 100401, https://doi.org/10.1016/j.coisb.2021.100401.
[17] J.M. Ubellacker, A. Tasdogan, V. Ramesh, B. Shen, E.C. Mitchell, M.S. Martin-Sandoval, Z. Gu, M.L. McCormick, A.B. Durham, D.R. Spitz, Z. Zhao, T.P. Mathews, S.J. Morrison, Lymph protects metastasizing melanoma cells from ferroptosis, Nature 585 (7823) (2020) 113–118, https://doi.org/10.1038/s41586-020-2623-z. Epub 2020/08/21, PubMed PMID: 32814895; PMCID: PMC7484468.
[18] G. Pascual, A. Avgustinova, S. Mejetta, M. Martin, A. Castellanos, C.S. Attolini, A. Berenguer, N. Prats, A. Toll, J.A. Hueto, C. Bescos, L. Di Croce, S.A. Benitah, Targeting metastasis-initiating cells through the fatty acid receptor CD36, Nature 541 (7635) (2017) 41–45, https://doi.org/10.1038/nature20791. Epub 2016/12/16, PubMed PMID: 27974793.
[19] C.J. Antalis, A. Uchida, K.K. Buhman, R.A. Siddiqui, Migration of MDA-MB-231 breast cancer cells depends on the availability of exogenous lipids and cholesterol esterification, Clin. Exp. Metastasis 28 (8) (2011) 733–741, https://doi.org/10.1007/s10585-011-9405-9. Epub 2011/07/12, PubMed PMID: 21744083.
[20] A. Nath, C. Chan, Genetic alterations in fatty acid transport and metabolism genes are associated with metastatic progression and poor prognosis of human cancers, Sci. Rep. 6 (2016), 18669, https://doi.org/10.1038/srep18669. Epub 2016/01/05, PubMed PMID: 26725848; PMCID: PMC4698658.
[21] H.Q. Ju, J.F. Lin, T. Tian, D. Xie, R.H. Xu, NADPH homeostasis in cancer: functions, mechanisms and therapeutic implications, Signal Transduct. Targeted Ther. 5 (1) (2020) 231, https://doi.org/10.1038/s41392-020-00326-0. Epub 2020/10/09, PubMed PMID: 33028807; PMCID: PMC7542157.
[22] V. Cracan, D.V. Titov, H. Shen, Z. Grabarek, V.K. Mootha, A genetically encoded tool for manipulation of NADP(+)/NADPH in living cells, Nat. Chem. Biol. 13 (10) (2017) 1088–1095, https://doi.org/10.1038/nchembio.2454. Epub 2017/08/15, PubMed PMID: 28805804; PMCID: PMC5605434.
[23] I. Elia, D. Broekaert, S. Christen, R. Boon, E. Radaelli, M.F. Orth, C. Verfaillie, T.G. P. Grünewald, S.M. Fendt, Proline metabolism supports metastasis formation and could be inhibited to selectively target metastasizing cancer cells, Nat. Commun. 8 (2017), 15267, https://doi.org/10.1038/ncomms15267. Epub 2017/05/11, PubMed PMID: 28492237; PMCID: PMC5437289.
[24] C.J. Aslakson, F.R. Miller, Selective events in the metastatic process defined by analysis of the sequential dissemination of subpopulations of a mouse mammary tumor, Cancer Res. 52 (6) (1992) 1399–1405. Epub 1992/03/15. PubMed PMID: 1540948.
[25] T. Schild, M.R. McReynolds, C. Shea, V. Low, B.E. Schaffer, J.M. Asara, E. Piskounova, N. Dephoure, J.D. Rabinowitz, A.P. Gomes, J. Blenis, NADK is activated by oncogenic signaling to sustain pancreatic ductal adenocarcinoma, Cell Rep. 35 (11) (2021), 109238, https://doi.org/10.1016/j.celrep.2021.109238. Epub 2021/06/17, PubMed PMID: 34133937.
[26] A.J. Minn, G.P. Gupta, P.M. Siegel, P.D. Bos, W. Shu, D.D. Giri, A. Viale, A. B. Olshen, W.L. Gerald, J. Massague, Genes that mediate breast cancer metastasis to lung, Nature 436 (7050) (2005) 518–524, https://doi.org/10.1038/nature03799. Epub 2005/07/29, PubMed PMID: 16049480; PMCID: 1283098.
[27] K.T. Yeung, J. Yang, Epithelial-mesenchymal transition in tumor metastasis, Mol. Oncol. 11 (1) (2017) 28–39, https://doi.org/10.1002/1878-0261.12017. Epub 20161209, PubMed PMID: 28085222; PMCID: PMC5242415.
[28] J.H. Tsai, J. Yang, Epithelial-mesenchymal plasticity in carcinoma metastasis, Genes Dev. 27 (20) (2013) 2192–2206, https://doi.org/10.1101/gad.225334.113. PubMed PMID: 24142872; PMCID: PMC3814640.
[29] J. Massague, E. Batlle, R.R. Gomis, Understanding the molecular mechanisms driving metastasis, Mol. Oncol. 11 (1) (2017) 3–4, https://doi.org/10.1002/1878-0261.12024. PubMed PMID: 28085221; PMCID: PMC5423223.
[30] M. Sciacovelli, C. Frezza, Metabolic reprogramming and epithelial-to-mesenchymal transition in cancer, FEBS J. 284 (19) (2017) 3132–3144, https://doi.org/10.1111/febs.14090. Epub 20170521, PubMed PMID: 28444969; PMCID: PMC6049610.
[31] N.Y. Sun, M.H. Yang, Metabolic reprogramming and epithelial-mesenchymal plasticity: opportunities and challenges for cancer therapy, Front. Oncol. 10 (2020) 792, https://doi.org/10.3389/fonc.2020.00792. Epub 20200520, PubMed PMID: 32509584; PMCID: PMC7252305.
[32] J. Xu, W. Zhang, L. Tang, W. Chen, X. Guan, Epithelial-mesenchymal transition induced PAI-1 is associated with prognosis of triple-negative breast cancer patients, Gene 670 (2018) 7–14, https://doi.org/10.1016/j.gene.2018.05.089. Epub 20180523, PubMed PMID: 29802992.
[33] D. Padua, J. Massague, Roles of TGFbeta in metastasis, Cell Res. 19 (1) (2009) 89–102, 10.1038/cr.2008.316. PubMed PMID: 19050696.
[34] A. Perkins, K.J. Nelson, D. Parsonage, L.B. Poole, P.A. Karplus, Peroxiredoxins: guardians against oxidative stress and modulators of peroxide signaling, Trends Biochem. Sci. 40 (8) (2015) 435–445, https://doi.org/10.1016/j.tibs.2015.05.001. Epub 20150609, PubMed PMID: 26067716; PMCID: PMC4509974.
[35] G. Hoxhaj, I. Ben-Sahra, S.E. Lockwood, R.C. Timson, V. Byles, G.T. Henning, P. Gao, L.M. Selfors, J.M. Asara, B.D. Manning, Direct stimulation of NADP(+) synthesis through Akt-mediated phosphorylation of NAD kinase, Science 363 (6431) (2019) 1088–1092, https://doi.org/10.1126/science.aau3903. PubMed PMID: 30846598; PMCID: PMC7261235.
[36] B. Schrors, S. Boegel, C. Albrecht, T. Bukur, V. Bukur, C. Holtstrater, C. Ritzel, K. Manninen, A.D. Tadmor, M. Vormehr, U. Sahin, M. Lower, Multi-omics characterization of the 4T1 murine mammary gland tumor model, Front. Oncol. 10 (2020) 1195, https://doi.org/10.3389/fonc.2020.01195. Epub 20200723, PubMed PMID: 32793490; PMCID: PMC7390911.
[37] A.P. Gomes, D. Ilter, V. Low, A. Rosenzweig, Z.J. Shen, T. Schild, M.A. Rivas, E. E. Er, D.R. McNally, A.P. Mutvei, J. Han, Y.H. Ou, P. Cavaliere, E. Mullarky, M. Nagiec, S. Shin, S.O. Yoon, N. Dephoure, J. Massague, A.M. Melnick, L. C. Cantley, J.K. Tyler, J. Blenis, Dynamic incorporation of histone H3 variants into chromatin is essential for acquisition of aggressive traits and metastatic colonization, Cancer Cell 36 (4) (2019) 402–417 e13, https://doi.org/10.1016/j.ccell.2019.08.006. Epub 2019/10/01, PubMed PMID: 31564638; PMCID: PMC6801101.
[38] D. Ray-Gallet, A. Woolfe, I. Vassias, C. Pellentz, N. Lacoste, A. Puri, D.C. Schultz, N. A. Pchelintsev, P.D. Adams, L.E. Jansen, G. Almouzni, Dynamics of histone H3 deposition in vivo reveal a nucleosome gap-filling mechanism for H3.3 to maintain chromatin integrity, Mol. Cell. 44 (6) (2011) 928–941, https://doi.org/10.1016/j.molcel.2011.12.006. PubMed PMID: 22195966.
[39] E. Szenker, D. Ray-Gallet, G. Almouzni, The double face of the histone variant H3.3, Cell Res. 21 (3) (2011) 421–434, https://doi.org/10.1038/cr.2011.14. Epub 2011/01/25, PubMed PMID: 21263457; PMCID: PMC3193428.
[40] W. Lu, L. Wang, L. Chen, S. Hui, J.D. Rabinowitz, Extraction and quantitation of nicotinamide adenine dinucleotide redox cofactors, Antioxidants Redox Signal. 28 (3) (2018) 167–179, https://doi.org/10.1089/ars.2017.7014. Epub 20170719, PubMed PMID: 28497978; PMCID: PMC5737638.
[41] X. Su, W. Lu, J.D. Rabinowitz, Metabolite spectral accuracy on orbitraps, Anal. Chem. 89 (11) (2017) 5940–5948, https://doi.org/10.1021/acs.analchem.7b00396. Epub 2017/05/05, PubMed PMID: 28471646; PMCID: PMC5748891.
[42] M. Yuan, S.B. Breitkopf, X. Yang, J.M. Asara, A positive/negative ion-switching, targeted mass spectrometry-based metabolomics platform for bodily fluids, cells, and fresh and fixed tissue, Nat. Protoc. 7 (5) (2012) 872–881, https://doi.org/10.1038/nprot.2012.024. Epub 2012/04/12, PubMed PMID: 22498707; PMCID: PMC3685491.
[43] A.G. Cox, A.G. Pearson, J.M. Pullar, T.J. Jonsson, W.T. Lowther, C.C. Winterbourn, M.B. Hampton, Mitochondrial peroxiredoxin 3 is more resilient to hyperoxidation than cytoplasmic peroxiredoxins, Biochem. J. 421 (1) (2009) 51–58, https://doi.org/10.1042/BJ20090242. Epub 2009/04/10, PubMed PMID: 19356151; PMCID: PMC3745641.
[44] N.H. Freese, D.C. Norris, A.E. Loraine, Integrated genome browser: visual analytics platform for genomics, Bioinformatics 32 (14) (2016) 2089–2095, https://doi.org/10.1093/bioinformatics/btw069. Epub 2016/03/16, PubMed PMID: 27153568; PMCID: PMC4937187.